# Thickness scaling of ferroelectricity in $BiFeO_3$ by tomographic atomic force microscopy

James J. Steffes[a,1], Roger A. Ristau[b], Ramamoorthy Ramesh[c,d,e], and Bryan D. Huey[a,b,2]

[a]Department of Materials Science and Engineering, University of Connecticut, Storrs, CT 06269; [b]Institute of Materials Science, University of Connecticut, Storrs, CT 06269; [c]Department of Materials Science and Engineering, University of California, Berkeley, CA 94720; [d]Department of Physics, University of California, Berkeley, CA 94720; and [e]Materials Science Division, Lawrence Berkeley National Laboratory, Berkeley, CA 94720

Edited by J. C. Séamus Davis, Cornell University, Ithaca, NY, and approved December 14, 2018 (received for review April 10, 2018)

**Nanometer-scale 3D imaging of materials properties is critical for understanding equilibrium states in electronic materials, as well as for optimization of device performance and reliability, even though such capabilities remain a substantial experimental challenge. Tomographic atomic force microscopy (TAFM) is presented as a subtractive scanning probe technique for high-resolution, 3D ferroelectric property measurements. Volumetric property resolution below 315 $nm^3$, as well as unit-cell-scale vertical material removal, are demonstrated. Specifically, TAFM is applied to investigate the size dependence of ferroelectricity in the room-temperature multiferroic $BiFeO_3$ across two decades of thickness to below 1 nm. TAFM enables volumetric imaging of ferroelectric domains in $BiFeO_3$ with a significant improvement in spatial resolution compared with existing domain tomography techniques. We additionally employ TAFM for direct, thickness-dependent measurements of the local spontaneous polarization and ferroelectric coercive field in $BiFeO_3$. The thickness-resolved ferroelectric properties strongly correlate with cross-sectional transmission electron microscopy (TEM), Landau–Ginzburg–Devonshire phenomenological theory, and the semiempirical Kay–Dunn scaling law for ferroelectric coercive fields. These results provide an unambiguous determination of a stable and switchable polar state in $BiFeO_3$ to thicknesses below 5 nm. The accuracy and utility of these findings on finite size effects in ferroelectric and multiferroic materials more broadly exemplifies the potential for novel insight into nanoscale 3D property measurements via other variations of TAFM.**

tomography | $BiFeO_3$ | AFM | ferroelectric | 3D

The room-temperature multiferroic $BiFeO_3$ has become a material of fundamental importance, owing to the single-phase intrinsic coupling of electric, magnetic, and strain order parameters (1, 2), as well as the tunability and scalability of electronic properties (3–5) and the magnetic exchange bias in $BiFeO_3$ thin films (6, 7). Integration of $BiFeO_3$ into functional devices necessitates a thorough understanding of finite size effects on critical materials properties such as ferroic order parameter coupling, spontaneous polarization and magnetization, and hysteretic coercivity. In $BiFeO_3$, film thickness has been shown to have a substantial impact on ferroelectric domain size and morphology (8–11); however, quantification of the thickness dependence of the switchable polarization is most critical for leveraging functionality from $BiFeO_3$. The thickness dependence of the spontaneous polarization in $BiFeO_3$ has been investigated using macroscopic measurements (12), surface-sensitive electron microscopies (13), and piezoresponse force microscopy (PFM) (14), although PFM has been the only technique employed thus far to explore the thickness dependence of the ferroelectric coercive field in $BiFeO_3$ below 40 nm (14–16). The results of these studies point toward a robust and stable switchable ferroelectric state in $BiFeO_3$ at thicknesses below 10 nm; however, such studies are limited by the uncertainties inherent in performing experiments on discretely fabricated samples, namely fluctuations in structure and composition resulting from the imperfect nature of thin-film synthesis.

Since its invention, PFM has been adopted as a scanning probe technique for high-resolution imaging and manipulation of ferroelectric domains at nanometer length scales. However, like most scanning probe methods, PFM is largely limited to 2D surface studies where imaging artifacts that arise from structural or chemical modifications to the film during scanning are necessarily minimized. Several optical approaches have been successful for tomographic imaging of ferroelectric domains in bulk $LaTiO_3$ and $LiNbO_3$ single crystals (17–19), although necessarily limited by optical resolution on the order of 500 nm in any dimension. In this article, we present a scanning probe method, tomographic atomic force microscopy (TAFM), for the nanoscale thickness-resolved measurement of ferroelectric domain geometry, spontaneous polarization, and the ferroelectric coercive field in an epitaxial 120-nm $BiFeO_3$ $(001)_{pc}$/$SrRuO_3$ $(001)_{pc}$/$DyScO_3$ $(110)_o$ thin-film heterostructure within a single imaging field of view. The subscripts "pc" and "o" denote pseudocubic and orthorhombic crystal axes, respectively. The ability to tomographically investigate the ferroelectric properties of $BiFeO_3$ within a single field of view (<20 μm) both minimizes the stoichiometric variability of the probed area and allows for high-accuracy $z$-position measurements of film thickness using the AFM. TAFM involves subtractive processing using the AFM probe with simultaneous acquisition of AFM images at progressively decreasing film thickness within a constant imaging area. This

## Significance

**Intrinsic and extrinsic properties of ferroelectric materials are known to have strong dependencies on electrical and mechanical boundary conditions, resulting in finite size effects at length scales below several hundred nanometers. In ferroelectric thin films, equilibrium domain size is proportional to the square root of film thickness, which precludes the use of present tomographic microscopies to accurately resolve complex domain morphologies in submicrometer films. We report a subtractive experimental technique with volumetric resolution below 315 $nm^3$, that allows for three-dimensional, tomographic imaging of materials properties using only an atomic force microscope. Multiferroic $BiFeO_3$ was chosen as a model system for illustrating the capabilities of tomographic atomic force microscopy due to its technological relevance in low-power, electrically switchable magnetic logic.**

Author contributions: J.J.S., R.R., and B.D.H. designed research; J.J.S. and R.A.R. performed research; J.J.S., R.A.R., and B.D.H. analyzed data; and J.J.S., R.R., and B.D.H. wrote the paper.

The authors declare no conflict of interest.

This article is a PNAS Direct Submission.



[1]Present address: Integration and Yield Engineering, GlobalFoundries, Hopewell Junction, NY 12533.

[2]To whom correspondence should be addressed. Email: bryan.huey@uconn.edu.

This article contains supporting information online at www.pnas.org/lookup/suppl/doi:10.1073/pnas.1806074116/-/DCSupplemental.

Published online January 25, 2019.

provides high-resolution (<50 nm) images and property measurements of subsurface structures throughout the thickness of a film. Employing TAFM, we report 3D PFM results, which provide quantitative 3D maps of the ferroelectric domain geometry in $BiFeO_3$ that strongly correlate with comparable cross-sectional transmission electron microscopy (TEM) analysis. The thickness dependence of the local piezoresponse acquired using TAFM has been analyzed in the context of Landau–Ginzburg–Devonshire phenomenological theory, which reveals the thickness dependence of the spontaneous polarization and critical switching thickness in $BiFeO_3$. Additionally, TAFM provides an experimental platform for thickness-dependent and defined-geometry experiments with site selectivity (20, 21). This capability is leveraged to perform polarization switching experiments on a programmed thickness gradient in $BiFeO_3$ following TAFM, and report localized, direct measurements of the electric field required for nucleation of ferroelectric domains as a function of film thickness. The thickness scaling of polarization switching in $BiFeO_3$ is found to obey the semiempirical Kay–Dunn scaling law to below 5 nm, which implies that ferroelectric switching in $BiFeO_3$ remains dominated by the electrostatics of the spontaneous polarization at nanometer length scales.

TAFM is the process in which a scanned probe, with downforces as high as micronewtons, performs mechanical removal (machining) of a specimen surface while simultaneously or sequentially recording one or more imaging modes, e.g., topography and PFM. The subtractive processing results in a series of conventional *x*-*y* plan-view images at continually increasing depths (decreasing film thickness, *h*), providing a 3D dataset of the desired imaging channel within the voided sample volume. Referenced to high-accuracy *x*, *y*, and *z* position data from the AFM, properties can thereby be volumetrically mapped throughout a portion or the entirety of a thin film. The concept is based on AFM micromachining methods previously reported for nanomechanical tooling (22–24) and fabrication of electron devices (25–27). The few reports of other TAFM variants have only characterized electrical conduction (28–30), and such methods are generally not applicable for high-modulus, electrically insulating materials such as ferroelectric oxides. Fig. 1*A* illustrates the application of TAFM for 3D PFM of ferroelectric domains throughout a multiferroic $BiFeO_3$ thin-film heterostructure. Fig. 1*A* depicts a single frame within a tomographic sequence, where the variable-thickness surface of $BiFeO_3$ has been created as a result of subtractive tomographic processing. The stripes shown in the $BiFeO_3$ film are ferroelectric/ferroelastic domains formed during film growth, with the direction of the spontaneous polarization indicated by red arrows. The subtractive nature of TAFM is apparent in *SI Appendix*, Fig. S1, which shows simultaneously acquired in-plane piezoresponse ($u_1^{\omega}$) and surface topography, i.e., $BiFeO_3$ film thickness (*h*) throughout an ∼200-frame tomographic sequence. The resulting topographic depression posttomography is shown in *SI Appendix*, Fig. S2. The mechanical dynamics of TAFM can be inferred from the 2D histogram in Fig. 1*C*, which shows a smoothly decreasing $BiFeO_3$ film thickness (*h*) starting at frame ∼25 and continuing for the remainder of the measured sequence. Here, the material removal rate remains relatively constant throughout the experiment (linear dependence between $BiFeO_3$ film thickness, *h*, and imaging frame); however, a substantial increase in topographic roughness and nonplanarity is observed ($\sigma = 0.2$ nm at $h = 120$ nm and $\sigma = 6.0$ nm at $h = 10$ nm) as the tomographic sequence progresses. These observations are visually confirmed in *SI Appendix*, Fig. S1*C*.

The applied probe downforce was selected to simultaneously enable the controlled removal of surface layers of $BiFeO_3$ while preventing mechanically induced ferroelectric or ferroelastic switching of ferroelectric domains (31), and to image within the strong indentation regime for optimization of PFM contrast via

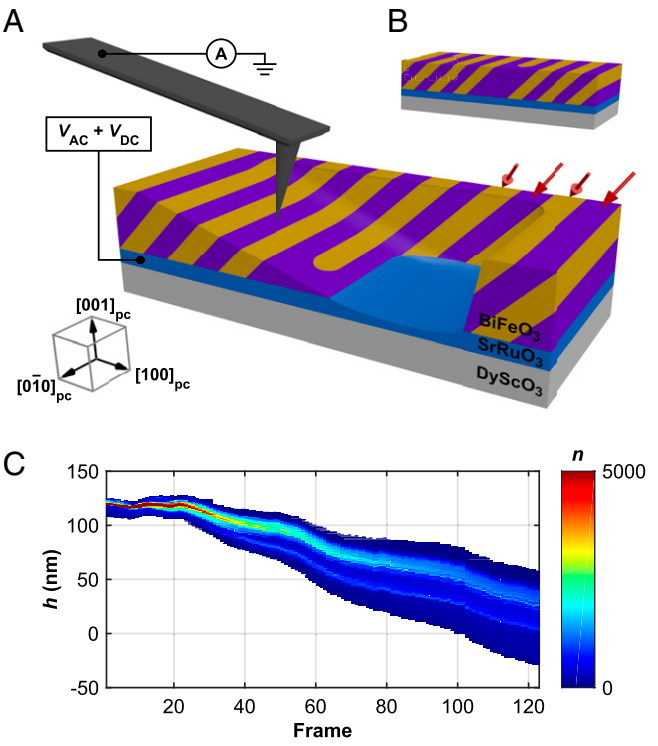


**Fig. 1.** TAFM of a $BiFeO_3/SrRuO_3/DyScO_3$ thin-film heterostructure. (*A*) PFM with probe current detection on a $BiFeO_3$ surface that has been prepared using TAFM, showing variable topography of $BiFeO_3$ and $SrRuO_3$ resulting from TAFM. Stripe-type contrast in $BiFeO_3$ represents ferroelectric domains with spontaneous polarization along $[\bar{1}1\bar{1}]_{pc}$ and $[\bar{1}\bar{1}1]_{pc}$, as indicated by red arrows. (*B*) Unprocessed, as-grown $BiFeO_3/SrRuO_3/DyScO_3$ heterostructure. (*C*) Two-dimensional histogram of *z* position as a function of imaging frame during TAFM of an $h = 120$ nm $BiFeO_3$ thin film.

minimization of nonlocal electrostatic interactions (32). Critical to the fidelity of TAFM measurements is the minimization of subsurface film damage during subtractive processing; any such damage would preclude accurate visualization and quantitative analysis of tomographic data. The relative frame-to-frame magnitude of the piezoresponse provides a continuous in situ indication of local crystal quality (14), which remained nearly constant during all TAFM scans on the $BiFeO_3$ film (*SI Appendix*, Figs. S1*A* and S3*A*); any subsurface defect formation or amorphization would result in suppressed piezoresponse relative to the as-grown film. In this work, an 11.4-μN mean probe downforce produced a mean vertical removal rate of 0.97 nm per frame (*SI Appendix*, Fig. S3*B*) and an overall tomographic sequence of ∼200 imaging frames on the $h = 120$-nm $BiFeO_3$ thin-film heterostructure. The in-plane piezoresponse increases slightly during the tomographic sequence commensurate with an increase in the mean probe downforce (32) (*SI Appendix*, Fig. S3*A*), both resulting from the broadening of the frame-to-frame surface roughness shown in Fig. 1*C*.

Fig. 2*A* superimposes three of the ∼200 sequential PFM images at mean *z* heights (film thickness, h) of 120 nm (frame 1), 77.8 nm (frame 65), and 33.8 nm (frame 120). For each of these frames, the in-plane piezoresponse ($u_1^{\omega}$) is overlaid as color contrast on the simultaneously acquired surface topography. As with the schematics in Fig. 1*A*, the stripe-type domain pattern in the PFM contrast indicates 71° ferroelectric/ferroelastic domains with polarization orientations $[\bar{1}1\bar{1}]_{pc}$ and $[\bar{1}\bar{1}1]_{pc}$. To produce an accurate tomogram from AFM data with temporally evolving *z* positions, a postprocessing reconstruction algorithm is employed to map the through-thickness PFM response of $BiFeO_3$ onto a 3D rectilinear grid with *x*, *y*, and *z* axes parallel to the $[100]_{pc}$, $[010]_{pc}$,

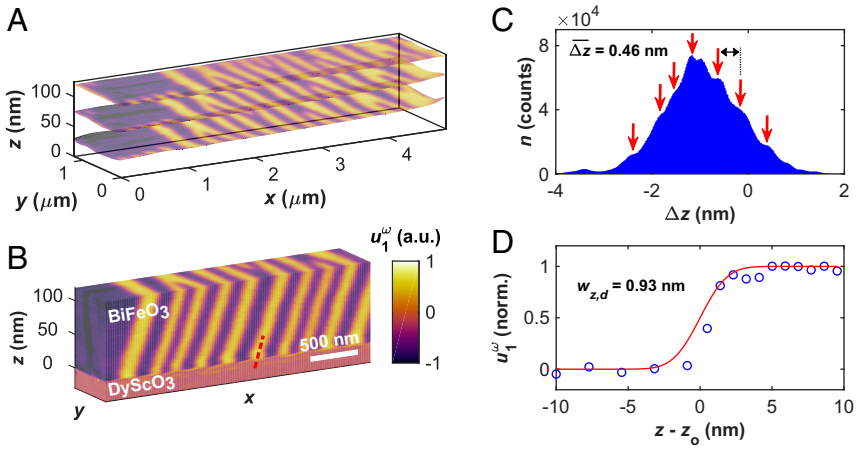


**Fig. 2.** Tomographic reconstruction of ferroelectricity from a $BiFeO_3$ thin-film heterostructure. Simultaneously acquired (*A*) PFM piezoresponse at $h = 120$ nm, $h = 77.8$ nm, and $h = 33.8$ nm from the ∼200-frame tomographic sequence superimposed onto the local surface topography (z position) for each imaging pixel. (*B*) Three-dimensional tomographic reconstruction of the thickness-resolved piezoresponse from a subregion of *A* (*z* dimension magnified ∼15× for viewing). (*C*) Histogram of the frame-to-frame change in the *z* position of the $BiFeO_3$ film surface ($\Delta z$), calculated on a per-pixel basis. Red arrows indicate apparent unit-cell steps in the fine structure of the histogram. (*D*) *z* resolution of tomographic PFM data calculated using the piezoresponse across the $BiFeO_3/SrRuO_3$ interface. The red line is an error function fit of the piezoresponse data (blue circles) centered around the interface, $z_o$.

and $[001]_{pc}$ crystal axes, respectively. The continuously decreasing, nonplanar *z*-position data obtained during TAFM cannot be accurately viewed in 3D due to the differential material removal rates throughout the imaging field of view (*SI Appendix*, Fig. S1*C*). Using simultaneously acquired *z*-position data, each (*x*, *y*, *z*) data point is used to translate the PFM response data onto a regular Cartesian grid using weighted trilinear interpolation within a standard 3D Delaunay triangulation routine. This procedure enables viewing and analysis of 3D data along correctly proportioned, pseudocubic crystal axes. To improve the accuracy of the *z* component of the tomogram, probe current is simultaneously measured to locally detect the zero-thickness position of the $BiFeO_3$ film, i.e., breakthrough to the conductive $SrRuO_3$ back electrode. The high conductivity of $SrRuO_3$ relative to $BiFeO_3$ provides a robust method for establishing the *z* position of the $BiFeO_3/SrRuO_3$ interface (*SI Appendix*, Fig. S4*C*), a critical parameter in the creation of spatially accurate tomograms constructed from AFM data. For reference, all *z*-position/film thickness (*h*) data presented in this work have been corrected for *z* drift and validated by setting the $BiFeO_3/SrRuO_3$ interface equal to $h = z = 0$.

Fig. 2*B* shows an isometric projection of a volumetric tomogram produced from a subsection of the reconstructed piezoresponse of $BiFeO_3$ shown in Fig. 2*A*. The *z* dimension in Fig. 2*B* is expanded by a factor of ∼15 for improved viewing of the *x*-*z* cross-sectional domain geometry. Both the 71° ferroelastic domain walls as well as "bifurcations" (i.e., defects) in the stripe pattern proceed throughout the entirety of the thickness of the film along the $[101]_{pc}$ direction (*SI Appendix*, Fig. S4*B*). A continuous *x* shift in the domain configuration of ∼−200 nm throughout the thickness of the $BiFeO_3$ film indicates that the domain walls are tilted relative to the $[001]_{pc}$ direction, an observation confirmed by TEM of equivalent specimens (4). At depths 120 nm below the as-grown surface (i.e., the $BiFeO_3$ film thickness, $z = 0$), an abrupt change in the PFM contrast from stripe-type domains to a uniform noise-limited signal indicates the complete removal of $BiFeO_3$ and the presence of either nonpiezoelectric $SrRuO_3$ or $DyScO_3$. The $BiFeO_3/SrRuO_3$ interface appears sharp and well-defined throughout the field of view in the tomograms of both piezoresponse and probe current. This is consistent with minimal subsurface structural damage during TAFM and is expected for the atomically precise interfaces commonly observed in epitaxial heterostructures synthesized using pulsed-laser deposition.

The vertical removal rate of 0.97 nm per frame during tomography of $BiFeO_3$ has been calculated using the mean *z* position of a given frame relative to the preceding frame; however, the large number of imaging pixels in the sequence ($n > 10^7$) permits a more precise analysis of material removal rate. A histogram of the frame-to-frame change in the *z* position of the film surface ($\Delta z$) for each *x*-*y* imaging pixel for all frames on $BiFeO_3$ is shown in Fig. 2*C*. A pronounced peak is observed at the mean removal rate, $\Delta z = -0.97$ nm; however, the fine structure of the distribution contains shoulder peaks with a mean spacing of 0.46 nm (red arrows), which is within ∼15% of the room-temperature *c*-axis lattice parameter of $BiFeO_3$ (4.0 Å). This finding strongly suggests that material removal occurs in discrete multiples of unit cells, providing evidence of near-atomic-scale subtractive fabrication capabilities of TAFM. The resolution of the 3D PFM data on $BiFeO_3$ has been calculated using the piezoresponse across both an in-plane domain wall and the $BiFeO_3/SrRuO_3$ interface. The actual width of a ferroelectric domain wall, as well as a heteroepitaxial interface, is on the order of 1–2 unit cells, and the apparent width of these atomically-sharp interfaces provides a quantitative measure of the PFM spatial resolution, comparable to edge resolution in optical microscopy (33). Fitting the interfacial piezoresponse with an error function results in an *x*-*y* spatial resolution of 18.7 nm (*SI Appendix*, Fig. S5) and a *z* spatial resolution of 0.93 nm, shown in Fig. 2*D*. The $BiFeO_3/SrRuO_3$ interface used to quantify the *z* resolution is indicated with the dashed red line in Fig. 2*B*, and $z_o$ is the location of the interface. These resolution figures result in a PFM spatial resolution and voxel size of less than 315 $nm^3$ and 20 $nm^3$, respectively, among the highest reported 3D resolution for materials properties to date.

To verify the spatial fidelity of the tomographic PFM data, TEM was performed on the $BiFeO_3$ film following TAFM. Fig. 3*A* shows a representative *x*-*z* cross-section of the tomogram from Fig. 2*B* with correctly proportioned axes. The white reference line in Fig. 3*A* is tilted at 40° from the $[100]_{pc}$ (*x*) crystal axis, and is shown to illustrate the vertical tilt of the 71° ferroelastic domain walls resolved by tomographic PFM. Fig. 3*B* shows a TEM cross-section taken along the $[010]_{pc}$ zone axis (*y* direction, Fig. 2*B*), an identical perspective as Fig. 3*A*, where the white arrow indicates both the location of a 71° domain wall and a 40° domain wall inclination angle. Fig. 3*B* has been acquired from a region of $BiFeO_3$ where TAFM first partially removed the $BiFeO_3$ film above the imaging field of view. The as-grown

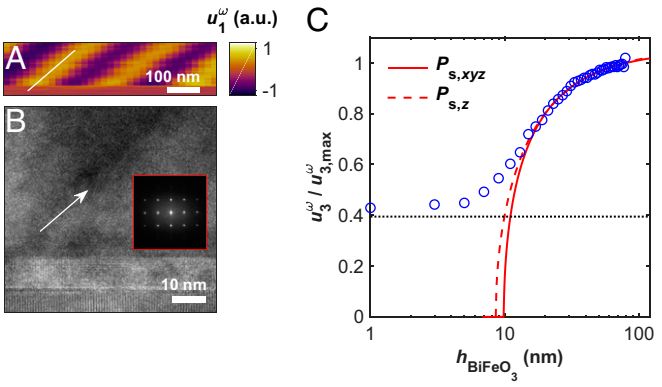


**Fig. 3.** Validation of TAFM using high-resolution TEM and phenomenological theory. (*A*) *x-z* cross-section of tomographic PFM data depicting the true geometry of a 71° ferroelastic domain wall. (*B*) Cross-sectional TEM of $BiFeO_3$ showing an equivalent 71° domain wall with identical geometry, obtained below a TAFM processed surface. (*Inset*) The 2D fast Fourier transform from $BiFeO_3$ adjacent to the domain wall. (*C*) Semilogarithmic plot of normalized piezoelectric displacement as a function of thickness for $BiFeO_3$, with nonlinear regressions for 3D and one-dimensional LGD phenomenological models. Horizontal dashed line in *C* indicates the PFM signal noise floor.

tilting of 71° ferroelastic domain walls as well as the crystallinity of the $BiFeO_3$ (fast Fourier transform; Fig. 3*B*, *Inset*) are readily observed in Fig. 3*B*, establishing the complementarity of TAFM and TEM imaging techniques. Combined with the faithful reproduction of the domain wall geometry and the near-constant piezoresponse magnitude throughout the $BiFeO_3$ film (Fig. 3*A*), these observations provide evidence of the effectiveness of TAFM measurements for accurate, high-resolution 3D imaging of ferroelectric domains.

Using TAFM, the thickness dependence of the spontaneous polarization in $BiFeO_3$ has been investigated within a single imaging field of view and validated with Landau–Ginzburg–Devonshire (LGD) phenomenological theory. The normal [001] component of the piezoelectric strain tensor in a piezoelectric crystal, $x_{33}$, is proportional to its spontaneous polarization, which in turn is a function of crystal thickness according to a 3D formulation of the LGD theory (13) (*SI Appendix*). Under the assumption of constant dielectric permittivity and electrostriction within the $BiFeO_3$ thickness range considered, the piezoelectric strain provides a measurement of the thickness-dependent spontaneous polarization in a ferroelectric such as $BiFeO_3$. Reformulating $x_{33}$ in terms of the out-of-plane cantilever displacement measured during PFM at frequency $\omega$ ($u_3^\omega$), the thickness dependence of the normalized piezoelectric displacement can be expressed as

$$\frac{u_3^\omega}{u_{3,\max}^\omega} = 2Q_{33}\epsilon_0\epsilon_{33}V^\omega \cdot A\sqrt{B+\sqrt{1-\frac{h_{cr}}{h}}}, \qquad [1]$$

where $\varepsilon_0$ is vacuum permittivity, $Q_{33}$ and $\varepsilon_{33}$ are *z*-oriented components of the electrostriction and dielectric permittivity tensors, respectively, $V^\omega$ is the oscillating PFM excitation voltage, $A$ and $B$ are temperature-dependent constants that incorporate multiple coefficients from the Landau free-energy expansion with respect to spontaneous polarization (13), and $h_{cr}$ is the critical thickness for ferroelectricity, i.e., the thickness below which a switchable, spontaneous polarization is theoretically no longer stable. Fig. 3*C* (open circles) shows the normalized, $[001]_{pc}$-oriented piezoresponse ($u_3^\omega$) for $BiFeO_3$ plotted as a function of film thickness, $h$, acquired following TAFM (source data shown in *SI Appendix*, Fig. S6). A nonlinear least-squares regression of $u_3^\omega$ versus $h$ using the model in Eq. **1** (Fig. 3*C*, solid line) results in a critical thickness, $h_{cr}$, of 6.8 nm, which is comparable to that calculated for $BiFeO_3$ by Rault et al. (13) (5.6 nm) using a combination of low energy and photoemission electron microscopy measurements. A fit of the data according to the one-dimensional LGD model derived by Maksymovych et al. (14) has been overlaid in Fig. 3*C* (dashed line) for reference. Deviation of the experimental piezoresponse from LGD theory can be partially attributed to a lower limit of measurable piezoresponse established by signal noise (dashed black line in Fig. 3*C*, $u_3^\omega/u_{3,\max}^\omega = 0.39$). The gradual approach to this limit is consistent with monotonically decreasing dielectric permittivity below an assumed constant (bulk) value at $BiFeO_3$ thicknesses below 15 nm.

In addition to tomographic measurements of ferroelectric properties, TAFM provides an experimental platform for investigating the local dynamics of thickness-dependent spontaneous polarization reversal (switching). Dual-frequency, time-dependent PFM with a superimposed dc bias voltage was used to both induce and spatially map the evolution of ferroelectric polarization switching (34) within a region of $BiFeO_3$ where a predefined thickness gradient has been intentionally fabricated through TAFM (Fig. 1*A*). Fig. 4*A* displays a topographic map of a smoothly varying $BiFeO_3$ thickness gradient, 60 nm > $h$ > 0 nm (i.e., $SrRuO_3$). Atomic-resolution high-angle annular darkfield scanning transmission electron microscopy (HAADF-STEM) for an equivalent region of $BiFeO_3$ is displayed in Fig. 4*B* and confirms the unperturbed crystal structure following TAFM at $h$ = 7 nm. There is no visible dislocation formation, amorphization, or $BiFeO_3/SrRuO_3$ layer intermixing (*SI Appendix*, Fig. S7), and the pseudocubic lattice structure is clearly visible to within a single unit cell of the $BiFeO_3$ surface. Starting with a dc voltage of +0.6 V dc, the bias voltage was held constant until the spatial distribution of $P^+$ and $P^-$ domains (out-of-plane PFM phase, $\phi_3^\omega$) within the field of view was invariant with respect to time (*SI Appendix*, Fig. S8). Following this criterion, the dc voltage was increased by 200 mV to induce further $P^- \rightarrow P^+$ polarization switching at thicker regions of $BiFeO_3$. This procedure was repeated until the out-of-plane ferroelectric polarization state had completely switched from $P^-$ to $P^+$ within the imaging field of view (+2.8 V dc). From this sequence, a nanoscale map of the local coercive voltage, $V_c$, can be constructed, shown in Fig. 4*C*.

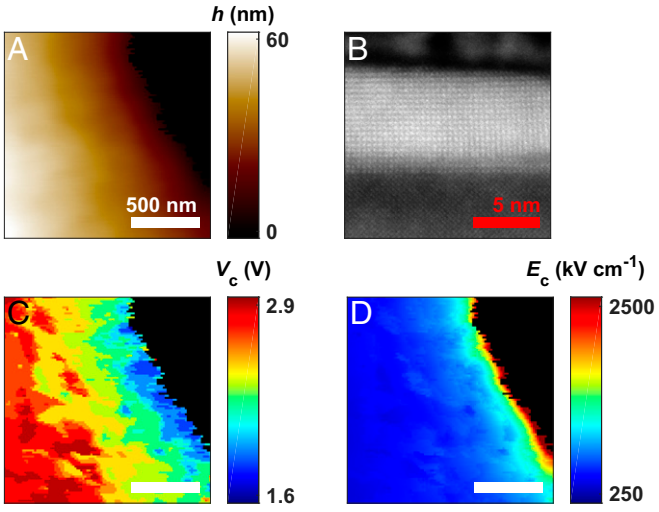


**Fig. 4.** Spatially resolved polarization switching of variable-thickness $BiFeO_3$ following TAFM. (*A*) $BiFeO_3$ film thickness ($h$) and (*B*) cross-sectional HAADF-STEM of $BiFeO_3$ following TAFM showing unperturbed crystal structure. (*C*) Coercive voltage, $V_c$ and (*D*) coercive field, $E_c$ cospatial with *A*, determined at the onset of ferroelectric switching from $P^-$ to $P^+$ polarization.

Coupling the spatially resolved $V_c$ with the local $BiFeO_3$ thickness ($h$, Fig. 4*A*) enables the ferroelectric coercive field, $E_c$, to be mapped with nanometer-scale resolution, shown in Fig. 4*D*. This approach allows direct visualization of the thickness dependence $E_c$ within a single imaging field of view. Clearly visible from these results is the direct proportionality of $V_c$ and $h$ (Fig. 4*C*) and the strong inverse proportionality of $E_c$ and $h$ for $BiFeO_3$ (Fig. 4*D*).

The nucleation-based polarization reversal model of ferroelectrics proposed by Landauer (35) and Kay and Dunn (36) defines the thickness dependence of the electric field required to nucleate a semiprolate spheroidal domain of opposite polarization in a uniformly polarized crystal. The nucleation field obeys the semiempirical equation

$$E_n = k\left(\frac{b^2 c}{a^3}\right)^{1/3} h^{-2/3}, \qquad [2]$$

where $E_n$ is the coercive field at domain nucleation, $k$ is a fixed constant, $a$, $b$, and $c$ are constants that describe the geometry of the domain nucleus, and $h$ is the crystal thickness. Several studies have reported Kay–Dunn coercive field scaling (i.e., $E_c \propto h^{-2/3}$) in thin-film ferroelectrics (37, 38), while others have observed more general inverse power-law correlations between coercive field and film thickness (14, 39); all scaling experiments to date have been performed across multiple samples having discrete film thicknesses. Deviation from Kay–Dunn scaling in ultrathin films ($h$ < 20 nm) has been attributed to perturbations in the depolarizing field acting antiparallel to the applied electric field (40), as well as a transition to cylindrically shaped domain nuclei at film thicknesses below 15 nm (41). Here, the spatially resolved $h$, $V_c$, and $E_c$ data shown in Fig. 4 provide the basis for a comprehensive statistical analysis of the thickness dependence of ferroelectric coercivity in $BiFeO_3$. Fig. 5*A* shows a plot of $V_c$ versus $h$ for $BiFeO_3$ calculated using TAFM; closed blue circles represent the median thickness for all pixels that have switched from $P^-$ to $P^+$ at the corresponding applied voltage, $V_c$. The spatially resolved ferroelectric switching permits the identification of $V_n$ (i.e., $V_c$) and $h$ for individual $P^+$ domain nuclei (open blue circles), in accordance with the theories of Landauer, and Kay and Dunn (*SI Appendix*, Fig. S8*F*). Reformulating Eq. **2** in terms of $V_n$ and assuming $E_n = V_n/h$ produces the relation $V_n \propto h^{1/3}$, a nonlinear power-law ($Ax^b$) regression of nuclei-$V_c$ versus $h$ in Fig. 5*A* yields the exponent $b$ = 0.331 ± 0.045 for TAFM data (solid red line), in strong agreement with Kay–Dunn scaling. Macroscopic measurements of $V_c$ obtained from $d_{33}$ measurements on discrete $BiFeO_3$ thin-film capacitors are also shown (black squares), along with the corresponding $Ax^{1/3}$ fit (dashed red line) for comparative visualization. The $V_c$ offset between macroscopic and PFM data could result from several possible mechanisms. As with all PFM studies in ambient conditions as performed here, voltage losses at the tip–sample interface may occur due to parasitic capacitances (42). Differences in work function for patterned electrodes compared with the AFM probe may cause a voltage offset as well. But, the similarities acquired via PFM for discrete specimens (black squares, Fig. 5), over tens of thousands of data points in a single field of view (blue circles, Fig. 5), or from distinct PFM hysteresis loops on the same thickness gradient specimen (*SI Appendix*, Fig. S9), all indicate uniform if not completely negligible parasitic effects.

Fig. 5*B* shows a plot of $E_c$ versus $h$ in $BiFeO_3$ on logarithmic axes (same labeling as Fig. 5*A*); the strong linearity and precision of TAFM data relative to macroscopic measurements is apparent. A nonlinear power-law regression of nuclei-$E_c$ versus $h$ yields the exponent $b$ = −0.670 ± 0.038, again in strong agreement with Kay–Dunn scaling. The minimum switched thickness measured using TAFM is 4.2 nm, in good agreement with the critical thickness predicted by the LGD fit of $u_3^\varphi$ versus $h$ (6.8 nm, Fig. 3*C*). Equivalent scaling behavior, albeit with lower precision, is observed in spectroscopic piezoresponse hysteresis loops acquired at several discrete thicknesses within the same region of $BiFeO_3$ (Fig. 5*B*, *Inset* and *SI Appendix*, Fig. S9). The scatter from discrete samples or hysteresis loop measurements does not represent intrinsic limitations, but rather extrinsic mechanisms that are often unavoidable for distinctly grown specimens or even positions on a single specimen. For tomographic PFM-based results, on the other hand, such extrinsic effects may be minimized. A statistical treatment of the thickness dependence of ferroelectric properties of $BiFeO_3$ obtained through TAFM is presented in *SI Appendix*, Fig. S10.

TAFM, augmented by direct identification of domain nuclei as a function of applied voltage and film thickness during ferroelectric switching, has enabled the observation that $BiFeO_3$ demonstrates Kay–Dunn scaling of $E_c$ to below 5-nm thickness. This result is not immediately intuitive, since the stepwise polarization rotation known to occur in $BiFeO_3$ (2) is substantially different from the Ising-type polarization reversal in uniaxial ferroelectric materials (e.g., $BaTiO_3$) upon which the Landauer–Kay-Dunn theory is formulated. The Landauer–Kay-Dunn theory describes the electrostatics and geometry of ferroelectric domain nucleation; equivalent scaling in $BiFeO_3$ implies that its Bloch-like multistep polarization rotation is governed by the same electrostatic formulation of domain nucleation for Ising-type ferroelectrics. More specifically, the observed scaling of $E_c$ suggests that the ferroelectric domain nuclei in $BiFeO_3$ retain semiprolate spheroidal geometry and that the effects of the depolarizing field remain constant throughout the two decades of film thicknesses measured, ~1 nm < $h$ < 120 nm. These analyses of nanoscale ferroelectric behavior in $BiFO_3$ represent an AFM-based approach for fundamentally understanding the size dependence of functional materials properties. TAFM allows for scaling phenomena to be explored on a single sample within a single imaging field of view, providing a high level of statistical confidence by representing each imaging pixel as a discrete capacitor element. By combining the subnanometer thickness resolution of AFM with the direct identification of domain nuclei, this work presents direct visualization reported of Kay–Dunn scaling in a ferroelectric. Unambiguous determination of absolute film thickness and local properties enabled by TAFM complements mean-thickness methods by providing access to thickness-dependent phenomena with precision, with broad potential for application across a range of material systems and AFM measurement variations.

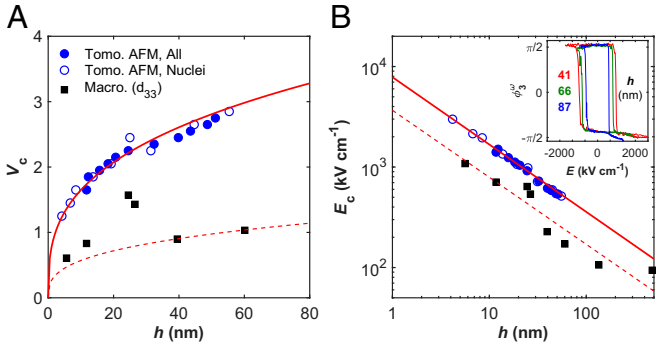


**Fig. 5.** Thickness dependence of the coercive voltage ($V_c$) and coercive field ($E_c$) in $BiFeO_3$. (*A*) $V_c$ vs. $h$, with TAFM data from all switched areas (closed blue circles), domain nuclei (open blue circles), and $d_{33}$-based measurements on macroscopic capacitor structures (black squares). Solid red line is a nonlinear power-law regression of $V_c$ vs. h. (*B*) Logarithmic plot of $E_c$ vs. $h$, using the same labeling convention as *A*. (*Inset*) Spectroscopic piezoresponse hysteresis loops (PFM phase) obtained at three discrete thicknesses following TAFM.

In conclusion, we report a volumetric scanning probe microscopy investigation of ferroelectricity across two decades of thickness in a single field of view for the multiferroic $BiFeO_3$. Using a tomographic variant of AFM in conjunction with PFM, the full 3D geometry of nanoscale ferroelectric domains has been resolved. By combining nanoscale mapping capabilities with site selectivity and subnanometer thickness resolution, TAFM establishes an experimental platform for direct, high-accuracy correlations between film thickness and material properties. In this article, TAFM has provided access to the thickness dependence of two critical ferroelectric properties, spontaneous polarization and ferroelectric coercive field, enabling clear confirmation of both LGD phenomenological theory and Landauer–Kay-Dunn coercive field scaling in $BiFeO_3$ with a critical thickness for ferroelectricity on the order of 5 nm. These results more broadly illustrate the potential of TAFM for future investigations into the thickness dependence of materials properties, as TAFM extends the constellation of scanning-probe-based local property mapping techniques into all three spatial dimensions with better than 315 $nm^3$ spatial resolution.

## Materials and Methods

$BiFeO_3$ $(001)_{pc}$/$SrRuO_3$ $(001)_{pc}$ heterostructures were grown epitaxially on $DyScO_3$ $(110)_o$ substrates using pulsed-laser deposition, with nominal thicknesses of 120 and 10 nm, respectively. Pulsed-laser deposition was performed at 690 °C in a 100-mTorr oxygen environment using a KrF laser at 8 Hz. AFM measurements were performed in ambient conditions with an Oxford Instruments Asylum Research Cypher S AFM, along with a Zurich Instruments HF2LI lock-in amplifier and NanoSensors (NanoWorld)-type CDT-NCHR conductive diamond-coated probes having nominal stiffness $k = 24$ N $m^{-1}$ and resonance frequency $f_0 = 325$ kHz.

**ACKNOWLEDGMENTS.** Y. H. Chu (National Chiao Tung University) and J. T. Heron (University of Michigan) fabricated the $BiFeO_3$ samples and provided macroscopic measurements, and A. Levin (University of Connecticut) performed ferroelectric domain identification for input into the variable-thickness switching analysis. All TEM imaging was performed using the facilities in the UConn/Thermo Fisher Scientific Center for Advanced Microscopy and Materials Analysis. J.J.S. acknowledges the GE-UConn Fellowship for Innovation for funding support. B.D.H. recognizes support from the Institute of Materials Science, University of Connecticut, and NSF:MRI:Development Award 1726862.

1. Heron JT, et al. (2011) Electric-field-induced magnetization reversal in a ferromagnet-multiferroic heterostructure. *Phys Rev Lett* 107:217202.
2. Heron JT, et al. (2014) Deterministic switching of ferromagnetism at room temperature using an electric field. *Nature* 516:370–373.
3. Chu YH, et al. (2009) Nanoscale control of domain architectures in BiFeO3 thin films. *Nano Lett* 9:1726–1730.
4. Jang HW, et al. (2009) Domain engineering for enhanced ferroelectric properties of epitaxial (001) BiFeO thin films. *Adv Mater* 21:817–823.
5. Johann F, Morelli A, Biggemann D, Arredondo M, Vrejoiu I (2011) Epitaxial strain and electric boundary condition effects on the structural and ferroelectric properties of BiFeO3 films. *Phys Rev B* 84:094105.
6. Martin LW, et al. (2008) Nanoscale control of exchange bias with BiFeO3 thin films. *Nano Lett* 8:2050–2055.
7. Béa H, et al. (2008) Mechanisms of exchange bias with multiferroic BiFeO3 epitaxial thin films. *Phys Rev Lett* 100:017204.
8. Catalan G, et al. (2008) Fractal dimension and size scaling of domains in thin films of multiferroic BiFeO3. *Phys Rev Lett* 100:027602.
9. Crassous A, Sluka T, Sandu CS, Setter N (2015) Thickness dependence of domain-wall patterns in BiFeO 3 thin films. *Ferroelectrics* 480:41–48.
10. Daumont CJM, et al. (2010) Tuning the atomic and domain structure of epitaxial films of multiferroic BiFeO3. *Phys Rev B* 81:144115.
11. Prosandeev S, Lisenkov S, Bellaiche L (2010) Kittel law in $BiFeO_3$ ultrathin films: A first-principles-based study. *Phys Rev Lett* 105:147603.
12. Kim DH, Lee HN, Biegalski MD, Christen HM (2008) Effect of epitaxial strain on ferroelectric polarization in multiferroic BiFe O3 films. *Appl Phys Lett* 92:12911.
13. Rault JE, et al. (2012) Thickness-dependent polarization of strained BiFeO3 films with constant tetragonality. *Phys Rev Lett* 109:267601.
14. Maksymovych P, et al. (2012) Ultrathin limit and dead-layer effects in local polarization switching of BiFeO 3. *Phys Rev B* 85:014119.
15. Shelke V, et al. (2012) Ferroelectric domain scaling and electronic properties in ultrathin BiFeO3 films on vicinal substrates. *New J Phys* 14:053040.
16. Chu YH, et al. (2007) Ferroelectric size effects in multiferroic BiFeO3 thin films. *Appl Phys Lett* 90:252906.
17. Cherifi-Hertel S, et al. (2017) Non-Ising and chiral ferroelectric domain walls revealed by nonlinear optical microscopy. *Nat Commun* 8:15768.
18. Haußmann A, et al. (2017) Three-dimensional, time-resolved profiling of ferroelectric domain wall dynamics by spectral-domain optical coherence tomography. *Ann Phys* 529:1700139.
19. Godau C, Kämpfe T, Thiessen A, Eng LM, Haußmann A (2017) Enhancing the domain wall conductivity in lithium niobate single crystals. *ACS Nano* 11:4816–4824.
20. Kolosov OV, Grishin I, Jones R (2011) Material sensitive scanning probe microscopy of subsurface semiconductor nanostructures via beam exit Ar ion polishing. *Nanotechnology* 22:185702.
21. Kutes Y, et al. (2017) Ion-damage-free planarization or shallow angle sectioning of solar cells for mapping grain orientation and nanoscale photovoltaic properties. *Nanotechnology* 28:185705.
22. Kim Y, Lieber CM (1992) Machining oxide thin films with an atomic force microscope: Pattern and object formation on the nanometer scale. *Science* 257:375–377.
23. Fang T-H, Weng C-I, Chang J-G (2000) Machining characterization of the nano-lithography process using atomic force microscopy. *Nanotechnology* 11:181–187.
24. Yan Y, et al. (2010) Top-down nanomechanical machining of three-dimensional nanostructures by atomic force microscopy. *Small* 6:724–728.
25. Magno R, Bennett BR (1997) Nanostructure patterns written in III-V semiconductors by an atomic force microscope. *Appl Phys Lett* 70:1855–1857.
26. Cortes Rosa J, et al. (1998) Direct patterning of surface quantum wells with an atomic force microscope. *Appl Phys Lett* 73:2684–2686.
27. Schumacher HW, Keyser UF, Zeitler U, Haug RJ, Eberl K (1999) Nanomachining of mesoscopic electronic devices using an atomic force microscope. *Appl Phys Lett* 75: 1107–1109.
28. Celano U, et al. (2015) Imaging the three-dimensional conductive channel in filamentary-based oxide resistive switching memory. *Nano Lett* 15:7970–7975.
29. Celano U, et al. (2014) Three-dimensional observation of the conductive filament in nanoscaled resistive memory devices. *Nano Lett* 14:2401–2406.
30. Luria J, et al. (2016) Charge transport in CdTe solar cells revealed by conductive tomographic atomic force microscopy. *Nat Energy* 1:16150.
31. Lu H, et al. (2012) Mechanical writing of ferroelectric polarization. *Science* 336:59–61.
32. Kalinin SV, Bonnell DA (2002) Imaging mechanism of piezoresponse force microscopy of ferroelectric surfaces. *Phys Rev B* 65:125408.
33. Kalinin SV, et al. (2006) Spatial resolution, information limit, and contrast transfer in piezoresponse force microscopy. *Nanotechnology* 17:3400–3411.
34. Huey BD, Nath Premnath R, Lee S, Polomoff NA (2012) High speed SPM applied for direct nanoscale mapping of the influence of defects on ferroelectric switching dynamics. *J Am Ceram Soc* 95:1147–1162.
35. Landauer R (1957) Electrostatic considerations in BaTiO3 domain formation during polarization reversal. *J Appl Phys* 28:227–234.
36. Kay HF, Dunn JW (1962) Thickness dependence of the nucleation field of triglycine sulphate. *Philos Mag* 7:2027–2034.
37. Chandra P, Dawber M, Littlewood PB, Scott JF (2005) Scaling of the coercive field with thickness in thin-film ferroelectrics. *Ferroelectrics* 313:7–13.
38. Ducharme S, et al. (2000) Intrinsic ferroelectric coercive field. *Phys Rev Lett* 84: 175–178.
39. Jo JY, et al. (2006) Polarization switching dynamics governed by the thermodynamic nucleation process in ultrathin ferroelectric films. *Phys Rev Lett* 97:247602.
40. Dawber M, Chandra P, Littlewood PB, Scott JF (2003) Depolarization corrections to the coercive field in thin-film ferroelectrics. *J Phys Condens Matter* 15:L393–L398.
41. Jo JY, Kim YS, Noh TW, Yoon JG, Song TK (2006) Coercive fields in ultrathin BaTiO3-capacitors. *Appl Phys Lett* 89:232909.
42. Yang CH, et al. (2009) Electric modulation of conduction in multiferroic Ca-doped BiFeO3 films. *Nat Mater* 8:485–493.